PHYSICAL REVIEW A **94**, 052702 (2016)

Quantum multiscattering interferences in collision-induced coherent electron emission from diatomic molecules by swift ion impact

H. Agueny[*] and J. P. Hansen[†]
Department of Physics and Technology, Allégaten 55, University of Bergen, N-5007 Bergen, Norway

(Received 4 August 2016; published 10 November 2016)

In the intramolecular scattering process, the interference between the rescattered electron waves emanating from each atomic center gives rise to additional oscillations superimposed on the Young-type oscillatory structure in the observed electron intensity. Here we explore numerically this behavior for coherent electron emission from the dimer $\mathrm{Rb_2}^+$ by fast-moving highly charged ions, which is achieved by solving the two-dimensional time-dependent Schrödinger equation. Well-defined modulations with higher frequency are observed in the momentum distribution of the ejected electron, which are well reproduced by additional quantitative calculations based on the third-order Born series. This demonstrates without ambiguity the dynamic interference induced by multiple scattering paths of the electron prior to emission. Furthermore, the dependence of the phenomenon on the emission direction of the electron and the orientation of the molecular axis also is investigated. The phenomenon is not specific to $\mathrm{Rb_2}^+$ as investigated in the present study, but is broadly applicable to other systems with sufficiently large internuclear distances, thus opening new prospects for the investigation of electron emission process from large systems.

DOI: 10.1103/PhysRevA.94.052702

I. INTRODUCTION

A system of two indistinguishable emitters such as a homonuclear diatomic molecule provides a source of spatial coherence, which is expected to be promising for information devices [1–3]. The coherent electron emission process generated by external beams from such a system enables one to explore elusive processes. Intramolecular scattering is one such process. The latter can lead to electron interference between rescattered waves emanating from each atomic center, giving rise to additional features beyond the Young-type oscillatory behavior that can be observed in the electron intensity. This is well known in solid physics as the extended x-ray-absorption fine-structure–type oscillations.

Recently, the phenomenon has been exploited in strong-field physics, specifically, in laser-induced electron scattering [4] and valence- and core-shell photoionization [5]. Moreover, the phenomenon was revisited in a series of experiments in the ion-impact-induced electron emission spectrum for different projectiles (H^+, F^{9+}, and Kr^{34+}) [6–8] and targets ($\mathrm{H_2}$ and $\mathrm{N_2}$) [8,9], as well as for a wide range of collision energy (from 1 to 63 MeV/nucleon) [6–8,10]. However, theoretical works based on nonperturbative approaches for $\mathrm{H_2}$ targets colliding with highly charged ions failed to reproduce the phenomenon [11,12]. Although an analytic model based on the second-order Born calculations [13] showed an enhancement of the differential ionization cross-section ratio at low electron velocities compared to the first-order prediction, a serious disagreement with the experimental findings has been found.

Our first linear dimensionality model [the one-dimensional (1D) model)] for energetic 63 MeV/nucleon H^+-$\mathrm{Rb_2}^+$ collisions demonstrates a clear signature of higher-harmonic components superimposed on the dominant first-order molecular double slit [14,15]. We have shown that the phenomenon emerges when the internuclear separation becomes sufficiently large so that electronic wave packets between the target centers can develop, resulting in multiscattering effects [15]. Motivated by these findings, we address here an extension to a 2D model to investigate this issue in more detail.

In this paper we explore this intriguing phenomenon by scrutinizing the ejected electron momentum distribution of the dimer $\mathrm{Rb_2}^+$ induced by fast 63 MeV/nucleon Kr^{34+} ions. This is achieved numerically by solving the 2D time-dependent Schrödinger equation (TDSE). In addition, we compare the full molecular treatment of the momentum distribution with coherent and incoherent atomic distributions, where the feedback effect of interfering waves between the two emitter sites during the intramolecular scattering is not included. This procedure allows one to identify the signature of this effect in a full molecular treatment. Furthermore, additional quantitative calculations based on the third-order Born series will be performed to support the presence of these effects. Their dependence on the emission direction of the electron as well as the orientation of the molecular axis also is explored. One of our main results is the emergence of pronounced high-harmonic components when the internuclear separation becomes larger than the de Broglie wavelength of the ejected electron.

The present paper is organized as follows. In Sec. II we introduce our nonperturbative approach to solve the 2D TDSE of dimers colliding with fast 63 MeV/nucleon highly charged ions, as well as an analytical model based on third-order Born series. The high-energy 63 MeV/nucleon has been chosen to be consistent with previous experimental [8,10] and theoretical [11,12] works and to maintain continuity with our previous one [15]. Section III is devoted to the analysis of the results and the comparison with additional calculations based on the independent-atom model and Born series. Atomic units $e = m_e = \hbar = 4\pi\varepsilon_0 = 1$ are applied except when stated otherwise.

---

[*] hicham.agueny@uib.no
[†] jan.hansen@uib.no

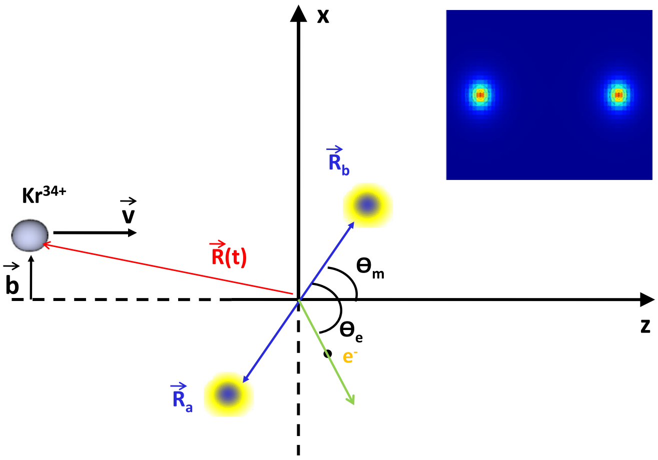

FIG. 1. Schematic diagram of the collision geometry of the projectile Kr^{34+} moving with the velocity v along the z axis and towards the fixed-in-space molecule ${Rb_2}^+$. Here θ_m is the orientation angle between the internuclear axis and the z axis, $\vec{R}(t)$ defines the relative motion between the projectile and target, and $\vec{b}$ is the impact parameter. The green arrow (e^-) indicates the electron emission direction with an ejected angle θ_e with respect to the molecular internuclear axis in z-x plane. The inset shows the contour of the initial electronic wave function density in the z-x plane of the z-aligned ($\theta_m = 0^\circ$) molecular ${Rb_2}^+$ at the equilibrium internuclear distance $R_{ab} = 9.2$ a.u.

II. THEORETICAL MODEL AND IMPLEMENTATION

A. Time-dependent Schrödinger equation calculations

We give a brief description of our numerical approach used to solve the 2D TDSE for fast Kr^{34+}-${Rb_2}^+$ collisions. The collision geometry is depicted in Fig. 1. We treat here the target molecule in the single-active-electron model with fixed internuclear distance. Under the straight-line trajectory approximation for the relative motion between the projectile and target, which is expressed as $\vec{R}(t) = \vec{b} + \vec{v}t$ (cf. Fig. 1), the TDSE governing the electron dynamics in a target generated by moving highly charged ions can be written as

$$\left[H_e(t) - i\frac{\partial}{\partial t}\right]\psi(\vec{r},t) = 0, \tag{1}$$

where $\vec{r} \equiv \{\vec{x},\vec{z}\}$ denotes the target electron coordinates. The electronic Hamiltonian $H_e(t)$ is expressed as

$$H_e(t) = -\tfrac{1}{2}\nabla^2 + V(r_a) + V(r_b) + V_p[|\vec{r} - \vec{R}(t)|], \tag{2}$$

where $\vec{r}_{a\,(b)} = \vec{r} - \vec{R}_{a\,(b)}$. Here $\vec{R}_a$ and $\vec{R}_b$ are the position vectors of the two target nuclei and $V(r_{a\,(b)})$ is the interaction potential between the electron and each target nucleus with the effective nuclear charge Z_{eff} and is parametrized in the form

$$V(r_{a\,(b)}) = -\frac{\alpha_1 + Z_{\text{eff}}e^{-\alpha_2 r_{a\,(b)}} + \alpha_3 r_{a\,(b)} e^{-\alpha_4 r_{a\,(b)}}}{r_{a\,(b)}}. \tag{3}$$

TABLE I. Parameters for the soft-core potentials in Eq. (3): E_{ion} is the ionization potential of the targets ${Rb_2}^+$ and Rb expressed in a.u.

	Targets	
Parameter	${Rb_2}^+$ ($R_{ab} = 9.2$ a.u.)	Rb
Z_{eff}	1.1268	1.0188
α_1	0.0313	0.0283
α_2	3.3319	3.3319
α_3	0.0356	0.0322
α_4	1.1379	1.1379
E_{ion}	0.2987	0.1604

This modified model potential, which originates from that proposed by Klapisch [16], is Coulombic at the origin and asymptotic and provides a correct binding energy. We found that a correct binding energy using this potential leads to an incorrect asymptotic form. However, calculations in one dimension [15] for varying forms of asymptotic strength parameters have shown that the emergence of high-order effects does not depend crucially on these parameters, while a correct binding energy is important. Using this form of potential with an appropriate choice of the parameters α_i ($i = 1,4$) gives a ${Rb_2}^+$ (Rb) binding energy of 0.2987 a.u. (0.1604 a.u.), which agrees well with that in Ref. [17] (see also [18]). These parameters are summarized in Table I. Here V_p is the Coulomb interaction between the projectile with the charge Z_p and the target electron,

$$V_p[|\vec{r} - \vec{R}(t)|] = -\frac{Z_p}{|\vec{r} - \vec{R}(t)|}. \tag{4}$$

The time evolution of the electronic wave function $\psi(\vec{r},t)$, which satisfies the TDSE [cf. Eq. (1)], is solved by a split-operator method based on the fast Fourier transform algorithm [19]. This is carried out on a square grid of size $|x| = |z| = 511.75$ a.u. with the spacing grid $\Delta x = \Delta_z = 0.25$ a.u., i.e., 2048 grid points along each axis direction. During the propagation scheme, the fast projectile Kr^{34+} having an energy of 63 MeV/nucleon (the corresponding velocity is $v \approx 50$ a.u.) evolves towards the positive z axis from its initial position $z_i = -250$ up to $z_f = 4100$ a.u., so the propagation time is $t_f = 82$ a.u. The time step used in the simulation is $\Delta t = 0.005$ a.u. An absorber is used to avoid artificial reflections due to a finite box size, but without perturbing the inner part of the wave function. At the end of the collision $t = t_f$, we calculate the momentum distribution of the ejected electron, for a given impact parameter, from the Fourier transform of the spatial ionization wave function. The latter is obtained by projecting the time-dependent wave packet onto the continuum states of the dimer targets, which is done by extracting the important bound states. Here we extract three bound states, since only these states are populated and are calculated accurately by solving the field-free Schrödinger equation using a Lagrange-mesh method with sinus basis functions [20]. The latter method was applied successfully to one-dimensional systems in our previous work [15]. We note that the momentum distributions discussed in the present work are integrated over the impact parameters ranging from 0 to 20 a.u.

B. Born calculations

In our previous work [15], the contribution of the second- and third-order amplitudes in the Born series were evaluated for a selected intermediate momentum $p_{1/2}$, which corresponds to an elastic process only in the continuum, i.e., $p_{1/2} = p$. Here the calculations have been extended to 2D spatial coordinates of the electron and integrated over the momenta p_1 and p_2. This can be written, for the contribution of the third-order amplitude, in the form

$$a^{(3)}(\vec{p}) = \iint d\vec{p}_1 d\vec{p}_2 [a^{(3),+}(\vec{p}_1,\vec{p}_2,\vec{p}) + a^{(3),-}(\vec{p}_1,\vec{p}_2,\vec{p})], \tag{5}$$

where the two partial amplitudes relate to forward (+) and backward (−) interatomic scattering. This can be expressed as

$$\begin{aligned} a^{(3),\pm}(\vec{p}_1,\vec{p}_2,\vec{p}) \sim & \int_{-\infty}^{t_2} dt_3 e^{i\Delta E_3 t_3} \langle \psi_p | V_s(r) | \psi_{p_2}^{\pm} \rangle \\ & \times \int_{-\infty}^{t_1} dt_2 e^{i\Delta E_2 t_2} \langle \psi_{p_2}^{\pm} | V_s(r) | \psi_{p_1}^{\pm} \rangle \\ & \times \int_{-\infty}^{t} dt_1 e^{i\Delta E_1 t_1} \langle \psi_{p_1}^{\pm} | V_p(t_1) | \psi_i \rangle, \end{aligned} \tag{6}$$

where $V_s(r) = V(r_a) + V(r_b)$ describes the electron-target interaction and ΔE_i $(i = 1,2,3)$ is the energy transfer to the electron.

To evaluate the amplitude in Eq. (6), we perform calculation based on different approximations, since a full evaluation of the scattering amplitude is a great challenge. Here, as in our previous 1D model, we assume that the term V_s is a screened Coulomb (or Gaussian) potential describing approximately the interaction between the electron and the two centers of the molecular target. The perturbation V_p is set constant and the initial state is chosen to be a superposition of a Gaussian wave packet $\varphi(r)$. The final and intermediate wave functions for electrons of momenta $\vec{p}$ and $\vec{p}_i$ $(i = 1,2)$, respectively, are approximated by plane waves and we assume that $\vec{p}_i$ propagates along the internuclear axis.

These plane-wave approximations allow us to get a simplified expression for the amplitude in Eq. (6). After integrating the time t and the electronic coordinate $\vec{r}$ in the formula (6), we get

$$\begin{aligned} a^{(3),\pm}(\vec{p}_1,\vec{p}_2,\vec{p}) \sim & \cos(\vec{Q}_\pm \cdot \vec{R}_{ab}/2) \cos(\vec{K}_\pm \cdot \vec{R}_{ab}/2) \\ & \times \cos(\vec{p}_1 \cdot \vec{R}_{ab}/2) \hat{V}(Q_\pm) \hat{V}(K_\pm) \hat{\varphi}(p_1), \end{aligned} \tag{7}$$

where $\vec{Q}_\pm = \vec{p} \pm \vec{p}_2$, $\vec{K}_\pm = \vec{p}_2 \pm \vec{p}_1$, and the factors $\hat{V}(\xi)$ $[\xi = (Q_\pm, K_\pm)]$ and $\hat{\varphi}(p_1)$ are the Fourier transforms of the scattering potentials and initial state, respectively.

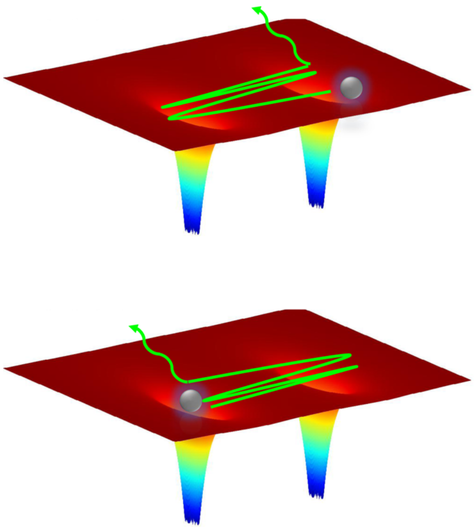

FIG. 2. Schematic diagram showing multiple scattering paths of the electron prior to emission from a symmetric double-well potential. Here the electron has an equal probability of being emitted from either the right atomic site (top) or the left site (bottom).

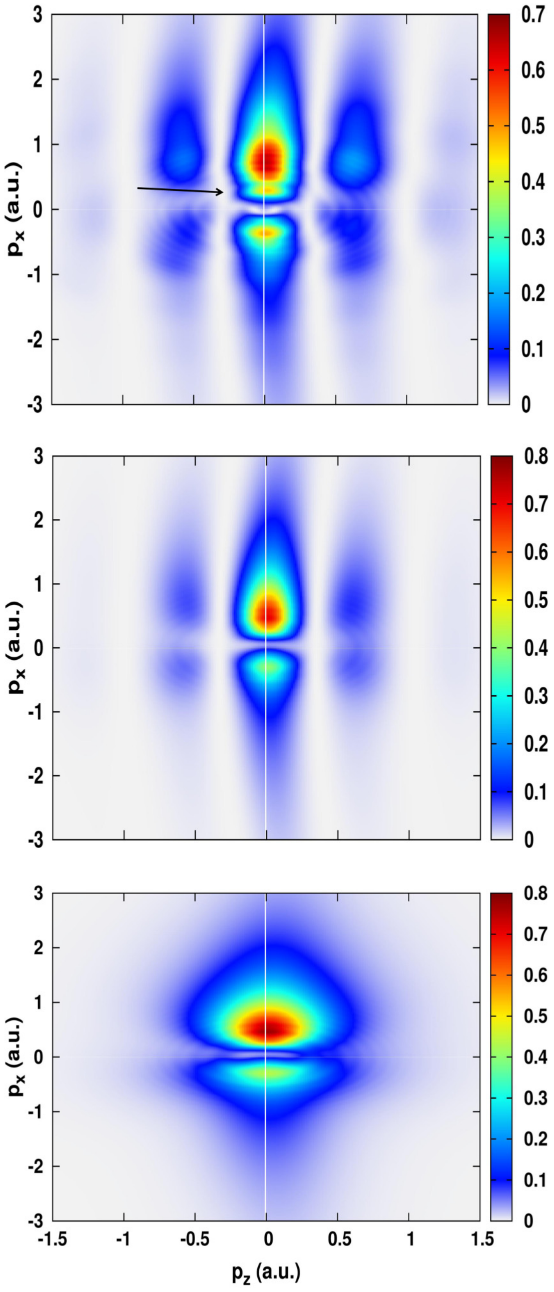

FIG. 3. Shown on top is the map of the ejected electron momentum distribution on the p_z-p_x plane for the electron emission process induced by 63 MeV/nucleon Kr^{34+} from the dimer Rb$_2^+$ aligned parallel ($\theta_m = 0°$) to the incoming ions (upper panel). Shown in the middle is the coherent 2Rb distribution mentioned in the text. Shown on the bottom is the incoherent atomic distribution.

The contribution of the third-order amplitude $a^{(3)}(\vec{p})$ is obtained by integrating over the momenta $\vec{p}_1$ and $\vec{p}_2$ according to Eq. (5). It contains indeed molecular structure information and reveals the important features of the interatomic scattering process. This is highlighted via the dependence on the internuclear separation R_{ab} as shown in Eq. (7). This model allows us to identify the high-order components in the spectrum of $\mathrm{Rb_2}^+$ that should be present in our TDSE calculations. We stress here that only the contributions of the second- and third-order amplitudes are analyzed. This is valid only as long as the nature and the origin of the high-order oscillations are explored [15].

III. RESULTS AND DISCUSSION

As mentioned in the Introduction, the main goal of the present work is to identify multiple scattering paths of the electron prior to emission, as depicted in Fig. 2. Highlighting components of these paths is challenging, since it requires scrutiny of the ejected electron spectrum, owing to the tiny oscillations superimposed on the clear Young-type ones.

To explore this intriguing phenomenon, we calculated the momentum distribution of the ejected electron in the p_z-p_x plane for an aligned $\mathrm{Rb_2}^+$ molecule parallel to the direction of the incoming Kr^{34+} ions. This is shown for an energy of 63 MeV/nucleon in the top panel of Fig. 3. Also shown is the coherent 2D distribution in the middle panel of the same figure. The latter distribution results from a coherent superposition of the ionization wave functions of each monomer separated by the same internuclear distance as in $\mathrm{Rb_2}^+$. We thus refer to this model as the 2Rb model, which takes into account only a single scattering process. It has the benefit of allowing us to identify in a full molecular treatment additional features associated with multiscattering effects. For reference, the corresponding incoherent atomic distribution is also shown in the bottom panel.

It can be clearly seen for the full molecular treatment $\mathrm{Rb_2}^+$ and the coherent 2Rb model that the momentum distribution exhibits the double-slit-like interference patterns. This is not the case, however, for the incoherent atomic distribution, which carries no double-slit structure information. It is interesting to note a peak shift away from $p_x = 0$ observed in atomic and molecular distributions. This results from the Coulomb focusing effect [21] on the ejected electron by the approaching Kr^{34+} ions. A similar effect has been observed in a slow ion-atom collision dealing with time-dependent calculations [22]. A closer inspection of the 2D electron ejected spectra reveals a

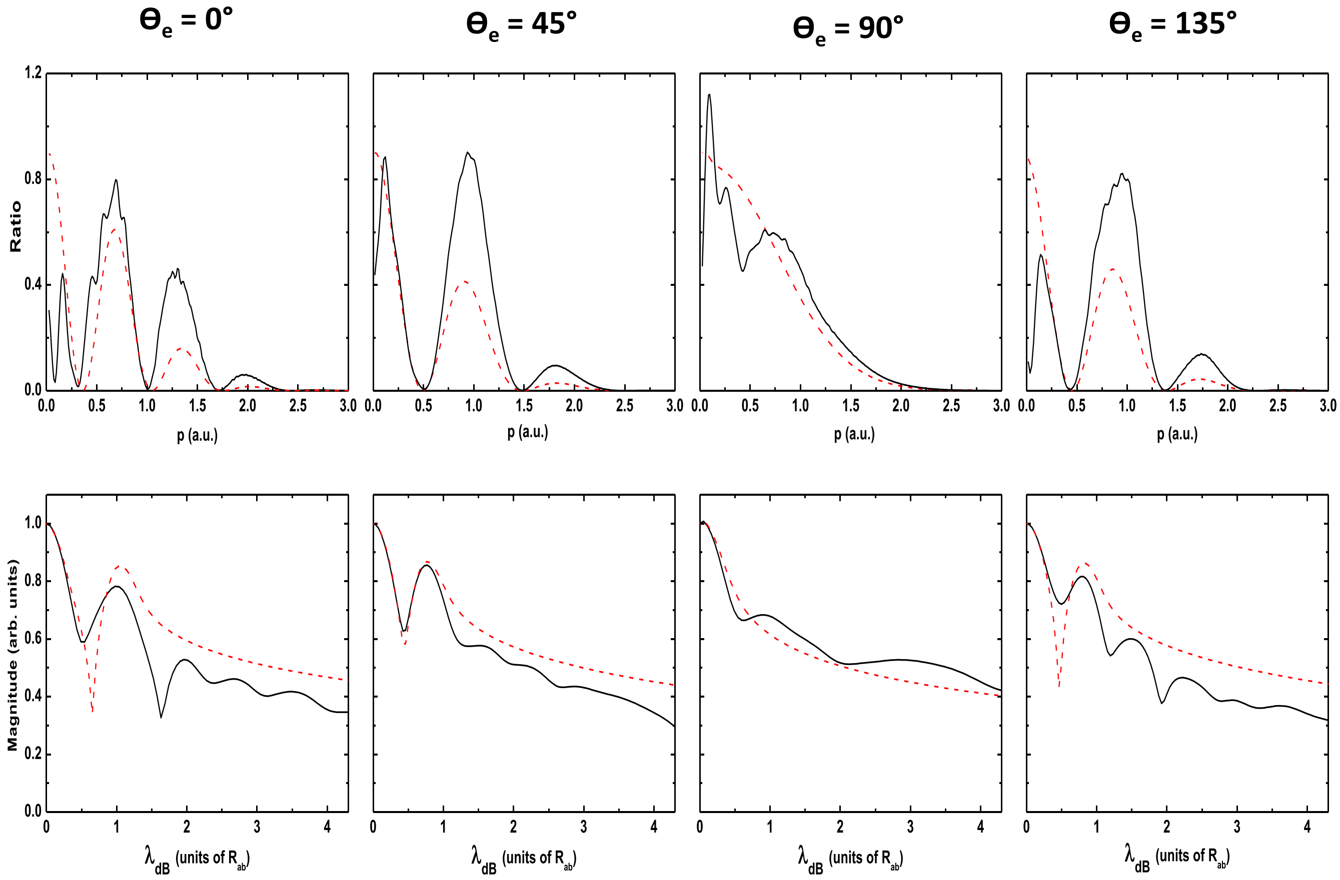

FIG. 4. Electron emission in 63 MeV/nucleon Kr^{34+}-$\mathrm{Rb_2}^+$ collisions for an aligned molecule parallel ($\theta_m = 0^\circ$) to the incoming ions. Calculations are performed for four emission angles, as indicated above the figure: $\theta_e = 0^\circ$, $\theta_e = 45^\circ$, $\theta_e = 90^\circ$, and $\theta_e = 135^\circ$. The top panels show the ratio of the momentum distributions for molecular ($\mathrm{Rb_2}^+$) and incoherent atomic (Rb) targets: black lines, full calculation; red dashed lines, results from the two-independent-atom (2Rb) model. Here the ratios have been convoluted by a Gaussian function (see the text). The bottom panels show the magnitude of the Fourier transform of the distribution ratios versus the de Broglie wavelength λ_{dB} (in units of the internuclear distance R_{ab}) of the ejected electron (black solid and red dashed lines are the same as in the top panels).

distinct structure present in $\mathrm{Rb}_2{}^+$ at low momenta, as indicated by a black arrow, but not in the 2Rb model. The observed structure must be attributed to the intramolecular scattering process, which is produced by interfering scattered electron waves emanating from each atomic center.

To retrieve the structural information regarding the intramolecular process with higher visibility, we examine the distribution ratios, i.e., the momentum distribution of the dimer $\mathrm{Rb}_2{}^+$ divided by the incoherent atomic distribution, for four fixed electron emission angles: in forward scattering 0°, 45°, and 90° and in backward scattering 135°. Results are displayed in the top panel of Fig. 4 and show a clear dependence of the ionization upon the electron emission angles.

We start with the case when the molecular interference fringes are expected to be more pronounced. This is the case when the two molecular centers are aligned with the momentum of the incoming ions and the emitted electron [23]. For this selected geometry, the distribution ratio for a full molecular treatment $\mathrm{Rb}_2{}^+$ (black solid lines) as a function of the ejected electron momentum is shown together with the corresponding coherent 2Rb distribution (red dashed lines). Well-defined modulations characteristic of Young-type interference are found in $\mathrm{Rb}_2{}^+$ spectra and are well reproduced by the 2Rb model. Nonetheless, a comparison between both distributions shows a remarkable feature of the $\mathrm{Rb}_2{}^+$ spectrum, which is the emergence of additional structures, which do not appear in the 2Rb model. A similar behavior is observed for all electron emission angles. Furthermore, a clear asymmetry between forward and backward electron emission is observed; this has been explained by a phase shift between the waves emitted by both centers [11]. Interestingly enough, at an observation angle of 90°, where no Young-type interferences are expected (at least in the momentum range considered here) as shown by the 2Rb model and mentioned previously (see, e.g., [11,24] for the theoretical works and [6,11,25,26] for the experimental results), more clear modulations are found. The emergence of these modulations is a clear consequence of the intramolecular scattering process in a full molecular treatment.

To identify the components of the high-order harmonics that provide insight into the multiple scattering paths of the electron prior to emission, we examine the Fourier transform of the distribution ratios displayed in the top panel of Fig. 4. As in our previous work, the distributions are convoluted by a Gaussian function that allows a faster decaying of the ratio for higher momenta [15]. Results are shown in the bottom panel of Fig. 4 and exhibit in addition to the first-order component signature of the direct emission clear components of high-order harmonics. It turns out that these components are more pronounced in backward emission (135°), in agreement with the experimental results [5], and become less pronounced in forward scattering. In the latter case, direct emission governs the scattering process and thus multiscattering effects become less probable.

For a detection angle of 90°, only a fingerprint of multiscattering effects is revealed. The observed features are supported by the featureless 2Rb model, which reveals only the characteristics of a single scattering as expected. It is important to note that the location of these higher-order components is sensitive to the electron emission angle. This sensitivity results from the fact that the high-order oscillations are superimposed on the first-order structures that dominate the electron emission process in forward scattering, as we mentioned before. However, one can expect a slight dependence on the backward direction. Furthermore, the location is found to be proportional to the internuclear distance R_{ab}, which can be linked, in the classical picture, to how many times the electron crosses the saddle before it gets ejected.

In order to validate our findings and to unambiguously associate the observed behavior in the ejected electron spectrum with multiscattering effects, additional calculations based on the high-order Born series are necessary. Here we perform calculations up to the third-order Born series. The Fourier transform of the contribution of the third-order scattering probability $|a^{(3)}(\vec{p})|^2$ [cf. Eq. (5)] is plotted in Fig. 5 (black dashed line) together with the corresponding second-order Born (blue dash-dotted line). As in our previous 1D model, the third-order contribution leads to an additional fourth component in the obtained spectrum, consistent with that which stems from the TDSE calculations for the $\mathrm{Rb}_2{}^+$ target. However, the comparison between both results shows a phase reversal for the two latter components. This may be caused by the scattering potential of the projectile, which is considered constant in Born calculations.

We conclude, therefore, that our findings demonstrate without ambiguity the origin of the high-order oscillations as a consequence of the dynamic interference between multiple scattering paths of the electron prior to emission.

For completeness, we show in Fig. 6 the dependence of this feedback effect of interfering waves upon the orientation of the molecular axis. Here an additional orientation is explored, i.e., $\mathrm{Rb}_2{}^+$ is aligned along the x axis ($\theta_m = 90°$, orange dashed lines) and compared with that for $\theta_m = 0°$ (black solid lines). Calculations of the distribution ratios are carried out for

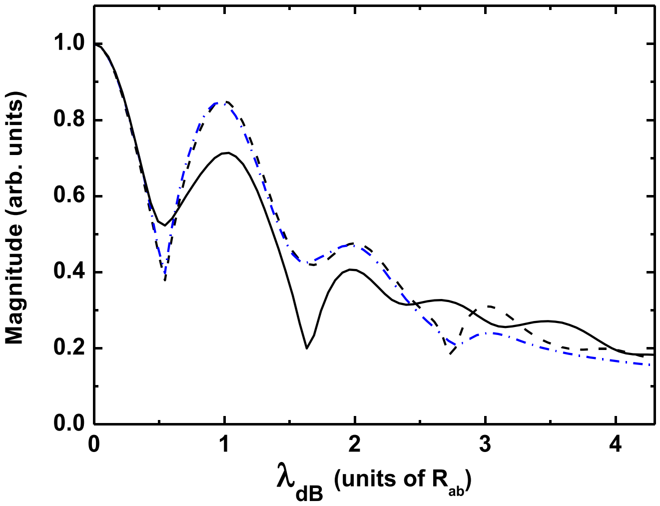

FIG. 5. Electron emission process in forward scattering ($\theta_e = 0°$) induced by 63 MeV/nucleon Kr^{34+} from $\mathrm{Rb}_2{}^+$ and for the molecular orientation axis $\theta_m = 0°$. The Fourier transform of the contributions of the second- (red dash-dotted line) and third-order [Eq. (5)] (black dashed line) Born scattering probabilities are plotted versus the de Broglie wavelength λ_{dB} (in units of the internuclear distance R_{ab}) of the ejected electron. The spectrum stemming from the TDSE (same as in the bottom panel of Fig. 4 on the left-hand side) is shown by a black line.

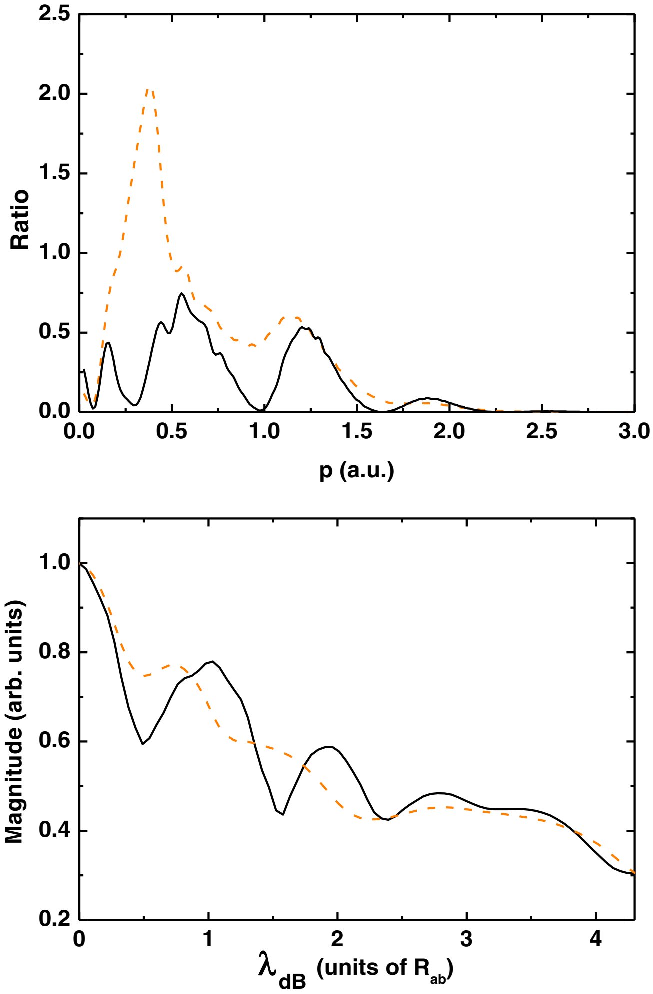

FIG. 6. Electron emission process in backward scattering ($\theta_e = 180^\circ$) induced by 63 MeV/nucleon Kr^{34+} from $\mathrm{Rb_2}^+$. Shown on top is the distribution ratios convoluted by a Gaussian function for two molecular orientation axes $\theta_m = 0^\circ$ (black solid lines) and $\theta_m = 90^\circ$ (orange dashed lines). The bottom shows the magnitude of the Fourier transform of the distribution ratios versus the de Broglie wavelength λ_{dB} (in units of the internuclear distance R_{ab}) of the ejected electron (black solid and orange dashed lines are the same as in the top panel).

backscattering emission ($\theta_e = 180^\circ$) and show well-defined modulations, which are somewhat smooth when the molecular axis is aligned perpendicular (see the top panel of Fig. 6). Their Fourier analysis shows once again a clear signature of a high degree of interference, although they are less pronounced when the molecule is aligned along the x axis ($\theta_m = 90^\circ$). In this geometry, the ionization comes mainly from one of the two emitter sites, specifically from the side where the impact parameter increases. In this case, the projectile experiences only one center and ionizes mainly from this site, which explains the observed behavior.

In order to reveal how the internuclear distance affects the multiscattering effects, we show in Fig. 7 calculations for three internuclear distances: $R_{ab} = 1.4$ a.u. (blue dashed lines), $R_{ab} = 5$ a.u. (red dash-dotted lines), and $R_{ab} = 10$ a.u. (black solid lines). We note here that all TDSE calculations were performed using the same form of the model potential [cf. Eq. (3)]. The results are shown for backscattering 135° emission, where the footprint of a high degree of intramolecular scattering is expected to be more pronounced. The distribution ratios exhibit distinct modulations that oscillate faster with increasing internuclear distance (see the top panel of Fig. 7). A Fourier transform of these distributions (see the bottom panel of Fig. 7) shows a strong dependence of the high-order harmonics on the internuclear distance, while at $R_{ab} = 1.4$ a.u. which corresponds to the internuclear distance of the $\mathrm{H_2}$ molecular target, no high-order components are revealed. At this distance, only a slight deflection of the first-order harmonic is found. The latter is located around the inverse momentum 0.24 a.u., as indicated by the blue arrow (see also the inset in the same figure). We stress here that a similar analysis

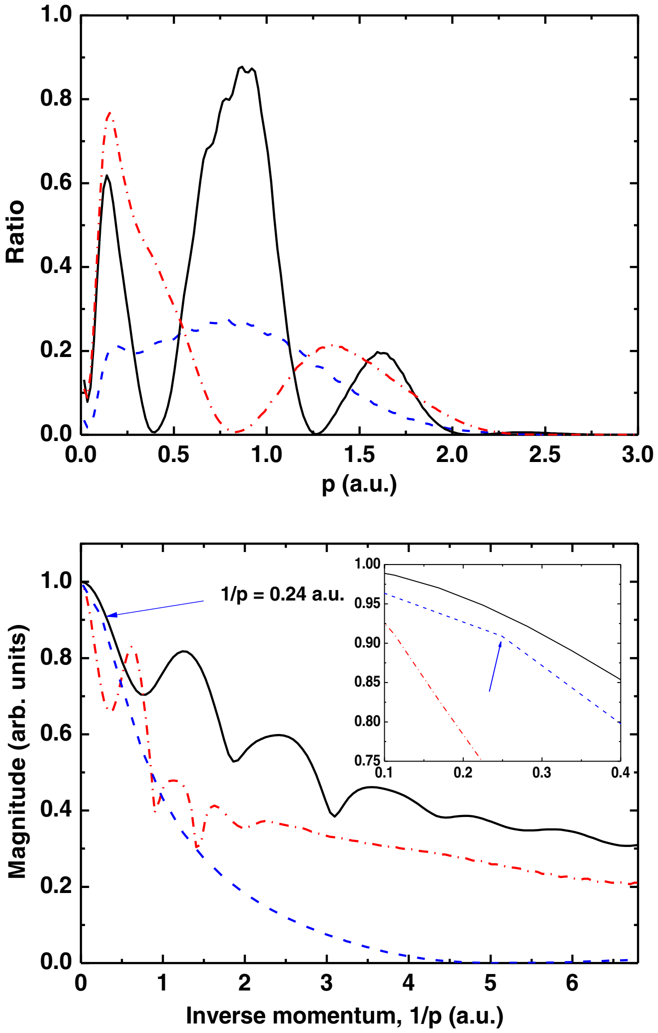

FIG. 7. Electron emission process in backward scattering ($\theta_e = 135^\circ$) induced by 63 MeV/nucleon Kr^{34+} from an aligned molecule $\mathrm{Rb_2}^+$ parallel to the incoming ions ($\theta_m = 0^\circ$). Shown on top are the distribution ratios for three internuclear distances R_{ab}: $R_{ab} = 1.4$ a.u. (blue dashed lines), $R_{ab} = 5$ a.u. (red dash-dotted lines), and $R_{ab} = 10$ a.u. (black solid lines). The bottom shows the magnitude of the Fourier transform of the distribution ratios versus the inverse momentum $1/p$ (in a.u.). The inset shows the magnification of the small part ($1/p < 0.4$ a.u.) of the spectrum (black solid, red dash-dotted, and blue dashed lines are the same as in the top panel).

performed experimentally by Tanis *et al.* [10] and reported for 60 MeV/nucleon Kr^{34+}-H_2 collisions does not reveal any component related to the first or second order for high-order harmonics. The authors, however, claimed that their analysis was focused only on higher-order frequencies.

Finally, although the impact energy dependence on the high-order effects has not been discussed here, their emergence is expected to be broadly applicable to other impact energies. We stress here that it has been shown that varying the latter parameter leads to a shift of minima originating from the Young-type oscillations, as well as a spectacular forward-backward asymmetry (see, e.g., [11]). Consequently, a shift of high-order components and a variation of their amplitudes can be expected, since they are superimposed on the Young-type oscillatory structures.

At this point, we conclude that our findings are a clear proof that the physical process leading to the emergence of the high-order components with higher visibility is linked mainly to the internuclear distance.

IV. CONCLUSION

In this work we have demonstrated a clear signature of a high degree of interference superimposed on the directly ejected electron waves from an aligned dimer generated by fast moving highly charged ions. This was achieved by solving the two-dimensional time-dependent Schrödinger equation nonperturbatively. The phenomenon is characterized by pronounced components with higher-order frequency on the electron ejected spectrum, which we validate by performing additional calculations based on a two-independent monomers model and third-order Born series. Such calculations help with the understanding of the mechanism behind the observed additional features in the ejected electron spectrum, which is linked to multiple scattering paths of the electron prior to emission. We have shown that the effect depends on the electron emission angle and alignment of the molecular axis and it varies substantially with the internuclear distance. The latter parameter can lead to additional components with higher visibility when it becomes larger than the de Broglie wavelength of the ejected electron. These findings, therefore, confirm our previous ones based on 1D calculations.

We believe that this study elucidates the issue surrounding the conditions of observing multiscattering effects with higher visibility, which would enhance our understanding of basic collision physics. This indeed will open new prospects for the investigation of electron emission from large systems, which can be considered as a starting point towards electron emission from solids generated by moving highly charged ions. We hope that our findings will lead to further experimental investigations of the phenomenon with large systems.

ACKNOWLEDGMENTS

We thank Alain Dubois for stimulating discussions. The research has received partial support from the NORDEN Top-Level Research Initiative: Energy efficiency with nanotechnology.

[1] K. Hosaka, H. Shimada, H. Chiba, H. Katsuki, Y. Teranishi, Y. Ohtsuki, and K. Ohmori, Phys. Rev. Lett. **104**, 180501 (2010).

[2] A. Micheli, G. K. Brennen, and P. Zoller, Nat. Phys. **2**, 341 (2006).

[3] E. S. Shuman, J. F. Barry, and D. DeMille, Nature (London) **467**, 820 (2010).

[4] J. Xu, C. I. Blaga, K. Zhang, Y. H. Lai, C. D. Lin, T. A. Miller, P. Agostini, and L. F. DiMauro, Nat. Commun. **5**, 4635 (2014).

[5] B. Zimmermann *et al.*, Nat. Phys. **4**, 649 (2008).

[6] S. Hossain, A. L. Landers, N. Stolterfoht, and J. A. Tanis, Phys. Rev. A **72**, 010701 (2005).

[7] D. Misra, A. H. Kelkar, S. Chatterjee, and L. C. Tribedi, Phys. Rev. A **80**, 062701 (2009).

[8] N. Stolterfoht, B. Sulik, B. Skogvall, J. Y. Chesnel, F. Frémont, D. Hennecart, A. Cassimi, L. Adoui, S. Hossain, and J. A. Tanis, Phys. Rev. A **69**, 012701 (2004).

[9] J. L. Baran, S. Das, F. Járai-Szabó, K. Póra, L. Nagy, and J. A. Tanis, Phys. Rev. A **78**, 012710 (2008).

[10] J. A. Tanis, J.-Y. Chesnel, B. Sulik, B. Skogvall, P. Sobocinski, A. Cassimi, J.-P. Grandin, L. Adoui, D. Hennecart, and N. Stolterfoht, Phys. Rev. A **74**, 022707 (2006).

[11] N. Sisourat, J. Caillat, A. Dubois, and P. D. Fainstein, Phys. Rev. A **76**, 012718 (2007).

[12] L. Sælen, T. Birkeland, N. Sisourat, A. Dubois, and J. P. Hansen, Phys. Rev. A **81**, 022718 (2010).

[13] K. Póra and L. Nagy, Nucl. Instrum. Methods Phys. Res. Sect. B **233**, 293 (2005).

[14] H. Agueny, A. Makhoute, A. Dubois, and J. P. Hansen, J. Phys.: Conf. Ser. **635**, 032094 (2015).

[15] H. Agueny, A. Makhoute, A. Dubois, and J. P. Hansen, Phys. Rev. A **93**, 012713 (2016).

[16] M. Klapish, Ph.D. thesis, Université Paris–Sud, 1969.

[17] M. Aymar, S. Azizi, and O. Dulieu, J. Phys. B **36**, 4799 (2003).

[18] http://www.nist.gov/pml/data/asd.cfm

[19] M. Feit, J. Fleck, Jr., and A. Steiger, J. Comput. Phys. **47**, 412 (1982).

[20] D. Baye, J. Phys. B **28**, 4399 (1995).

[21] T. Brabec, M. Y. Ivanov, and P. B. Corkum, Phys. Rev. A **54**, R2551 (1996).

[22] S. X. Hu, Phys. Rev. A **83**, 041401(R) (2011).

[23] A. Messiah, in *Quantum Mechanics* (North-Holland, Amsterdam, 1970), Vol. II, pp. 848–856.

[24] L. Nagy, L. Kocbach, K. Pora, and J. P. Hansen, J. Phys. B **35**, L453 (2002).

[25] N. Stolterfoht, B. Sulik, L. Gulyás, B. Skogvall, J.-Y. Chesnel, F. Frémont, D. Hennecart, A. Cassimi, L. Adoui, S. Hossain, and J. A. Tanis, Phys. Rev. A **67**, 030702 (2003).

[26] D. Misra, U. Kadhane, Y. P. Singh, L. C. Tribedi, P. D. Fainstein, and P. Richard, Phys. Rev. Lett. **92**, 153201 (2004).